Platinum(II) Complexes of Benzannulated N^N⁻^O-Amido Ligands: Bright Orange Phosphors With Long-Lived Excited States

Issiah B. Lozada,[a] *J. A. Gareth Williams,*[b,*] *and David E. Herbert*[a,*]

[a] Department of Chemistry and the Manitoba Institute for Materials, University of Manitoba, 144 Dysart Road, Winnipeg, Manitoba, R3T 2N2, Canada

[b] Department of Chemistry, Durham University, Durham, DH1 3LE, UK

*david.herbert@umanitoba.ca, j.a.g.williams@durham.ac.uk

ABSTRACT

The synthesis, structural characterization and photophysical properties of a series of platinum(II) complexes of benzannulated pincer-type diarylamido ligands are described. The ligands all contain tricyclic phenanthridine (3,4-benzoquinoline) rings as donor arms, which were elaborated into N^N⁻^O-coordinating chelates via partial condensation with acetylacetone. The proligands are easily deprotonated, and metallation can be achieved under mild conditions using simple Pt(II) salts and Ag_2O as a base. The resulting Pt(II) complexes exhibit strong metal-to-ligand charge-transfer absorptions in the region ~450-575 nm and are phosphorescent in solution at room temperature, emitting bright orange light (λ_{max} ~ 600 nm) with quantum yields of up to 16% and excited-state lifetimes on the order of ~20 μs. Computational modelling reveals that the lowest-lying triplet state is populated efficiently due to strong coupling between singlet and triplet excited state manifolds, as in related cyclometallated compounds of Pt(II). Substituents (CH_3, tBu, or CF_3) in the 2 position of the phenanthridine unit are found to have little influence on the optical properties, but the emission is severely quenched when a methyl substituent is introduced *ortho* to the coordinating nitrogen (position 6). Molecular distortions in the excited state are shown to be primarily responsible for the quenching in this complex.

Introduction

Emissive platinum(II) complexes have long been the subject of intensive investigation, thanks to the myriad potential applications of their phosphorescence including in light-emitting diodes,[1–4] imaging,[5–7] and sensing.[5,8,9] This ubiquity is owed both to the high spin-orbit coupling (SOC) constant of the 5d transition metal, which leads to efficient population of the triplet T_1 state through intersystem crossing and its subsequent radiative decay, and to a mature coordination chemistry in which ligand design can be used to control emission color and intensity.[10,11] Amongst the brightest Pt(II) emitters, multidentate cyclometallating ligands are common,[12] mostly ones that are derived from C-H activation of phenylpyridine derivatives and related molecules. With respect to tridentate analogs, C^N^N,[13–15] N^C^N[16,17] and C^N^C[18] architectures predominate. In these ligands, the synergy of strong σ-donation from Pt-C bonds and the π-accepting character of the heterocycle leads to the stabilization of charge-transfer (CT) excited states relative to metal-centered (MC) ones. The chelating ligand arrangement also increases molecular rigidity, which helps to suppress excited-state distortions that promote non-radiative decay processes deterimental to emission.[19]

N^N^N-donor scaffolds have also been reported, with monoanionic[20–22] ligands proffering expanded chelate ring sizes typically showing the strongest emission.[23] For example, $[Pt(dqpy)Cl]^+$, which incorporates two 6-membered chelate rings, shows considerably improved emission (τ = 16 μs, Φ_{lum} = 0.036 in dichloromethane)[24] compared to $[Pt(tpy)Cl]^+$, which is essentially non-emissive in solution {dqpy = 1,3-di(8-quinolyl)benzene; tpy = 2,2':4',6"-terpyridine}. There, introduction of 8-substituted quinoline donors relaxes the constraints placed on the ligand in adopting the preferred square-planar geometry of Pt(II), resulting in a nearly linear N-Pt-N bond angle of 178.8°, compared with the much more acute 163.5° in

[Pt(tpy)Cl]ClO_4.[25] The closer-to-optimal geometry strengthens the ligand field and boosts emission through suppressed non-radiative decay resulting from destabilized metal-centred excited states. Pt(II) complexes of N^N^O-coordinating tridentate ligands have also been reported. They include monoanionic scaffolds derived from 6-(*ortho*-phenoxy)bipyridines[26,27] as well as related Schiff-base pyridine-imine and pyridine-hydrazone phenolates.[28] The latter two feature one 5- and one 6-membered chelate ring.

We have been interested in incorporating benzannulated *N*-heterocycles into multidentate scaffolds in order to delineate design principles for tuning photophysical properties of transition metal complexes.[29,30] Our work to date has focused on phenanthridines (3,4-benzoquinolines). 2,4-Functionalized phenanthridines can be readily prepared via one-pot Pd-catalyzed cross-coupling/condensation reactions of 2-formylphenylboronic acids and a substituted aniline.[31] Here, we targeted (N^N^O)Pt(II) complexes of simple β-enaminoketonato architectures[32] bearing phenanthridinyl donor arms. Using ligands that are simple to prepare, complexation to Pt(II) can be achieved under similarly mild conditions. The complexes display quite bright orange emission at room temperature, with significantly improved quantum yields compared to those of related N^N^O-ligated systems.[26–28] Structure-property correlations indicate that substituents in the phenanthridinyl ligand impact on molecular rigidity rather than ligand electronics, confirmed by density functional theory (DFT) modelling of the lowest lying triplet excited states.

RESULTS AND DISCUSSION

Proligands **L1**-**L4** were prepared via acid-catalyzed condensation of the appropriately functionalized (4-amino)phenanthridine (**P1**-**P4**) with acetylacetone (Scheme 1) as previously described.[33,34] Platinum complexes **1**-**4** were obtained by refluxing a mixture of $PtCl_2$ and the respective proligands in THF in the presence of a Brønsted base. As for **3** and **4**,[33] we found the use of Ag_2O allowed for the highest yields. Subsequent work-up enabled isolation of bright orange solids in moderate (**1**, 34%; **2**, 49%) to high (**3**, 87%; **4**, 86%) yields. The lower solubility of **3** likely contributed to the reduced yield, while the increased steric congestion at the C_1 by introduction of a methyl group may have reduced conversion to **2**. All Pt(II) complexes were found to be stable to both air and ambient moisture. Coordination to Pt(II) induces a shift to higher frequency of the N=C_1H resonance observed by ^{1}H NMR (δC_1H: **L1**, 9.29 ppm; **1**, 10.04 ppm). Similarly, the ^{1}H resonance of the methyl-substituent at C_1 ($C_{20}H_3$) shifts to a higher frequency in **2** ($\delta C_{20}H$: **L2**, 3.05 ppm; **2**, 3.53 ppm). This characteristic shift of the C_1H ^{1}H resonance, and in the case of **2** the $C_{15}H$, C_1 is also diagnostic in other square-planar Pt(II) complexes supported by phenanthridine-based ligand frameworks.[21,22,33,35] Observation of coupling between the N=C_1H and spin-active ^{195}Pt (e.g., $^3J_{PtH}$ = 40 Hz in **1**) also supports binding of the phenanthridinyl donor to the metal centre. High resolution mass spectra (HRMS) of **1** and **2** are consistent with the proposed molecular formulae.

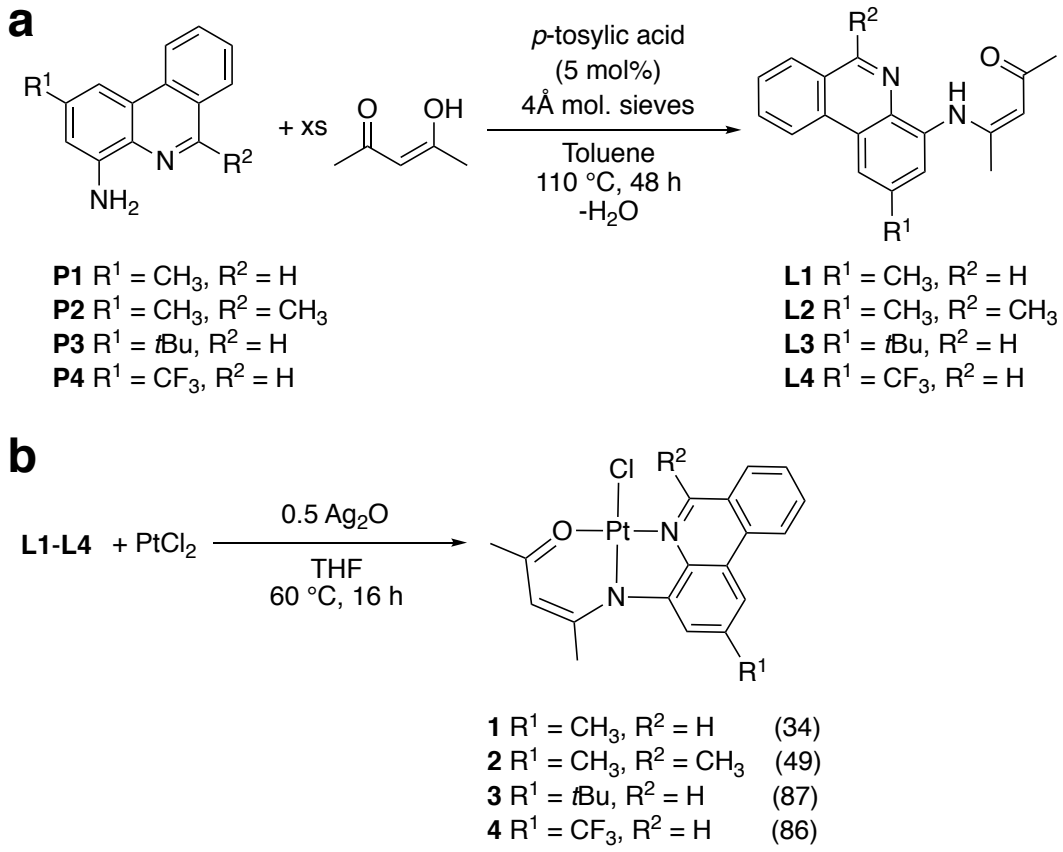

Scheme 1. Synthesis of proligands **L1**-**L4** and Pt complexes **1**-**4** with yields in parentheses.

The solid-state structures of three of the Pt(II) complexes were established using single-crystal X-ray diffraction (Figure 1; the structure of **3** has been previously reported[33]). In each complex, the Pt(II) ion is arranged in a pseudo-square planar coordination environment with the chloride ligand *trans* to the amido nitrogen donor. The fused tricyclic phenanthridinyl unit is more or less coplanar with the square coordination plane of Pt(II). Of the series, **2** exhibits a significant distortion as revealed by the angles of 19.5° (θ: Cl2–Pt2–N3–C21) and 30.6° (θ: Cl1–Pt1–N1–C1) between the phenanthridinyl and metal coordination planes due to the increased steric congestion arising from the methyl substituent at the C_1=N$^{\text{phenanthridinyl}}$ carbon. Accordingly, the calculated τ_δ value[36] for **2** is more in line with a distorted square-planar

coordination environment compared with **3** and **4** (τ_4^{δ} for **2**: 0.16; **1**: 03; **3**: 0.03; **4**: 0.02). Moreover, the N2–Pt1–Cl1 / N4-Pt2-Cl2 angles are smaller in **2** [168.24(10)° and 172.48(9)°, respectively, for the two molecules in the asymmetric unit] compared with **1** [177.45(17)°], **3** [176.70(11)°][33] or **4** [177.97(18)°]. These distortions in the ground state of **2** have implications for its photophysics (*vide infra*). The four proligands present NMR and IR spectra consistent with the keto-enamine tautomer predominating in solution.[33,34] In the Pt(II) complexes, the C-O distance is still quite short but does elongate slightly compared to the proligand (C17-O1 1.278-1.297 Å, *cf.* 1.244(3) in $^{t\mathrm{Bu}}$**LH**[33]), while the C16-N2 distance contracts (1.322-1.334 Å, *cf.* 1.363(3) in $^{t\mathrm{Bu}}$**LH**[33]), implying at least some C–O-Pt/C=N-Pt character. Indeed, the Pt1-N2 distances (1.998-1.987 Å) are not significantly different from unambiguous Pt-N_{imine} distances *trans* to chloro ligands reported for square-planar Pt(II) complexes with closely related coordination environments.[28]

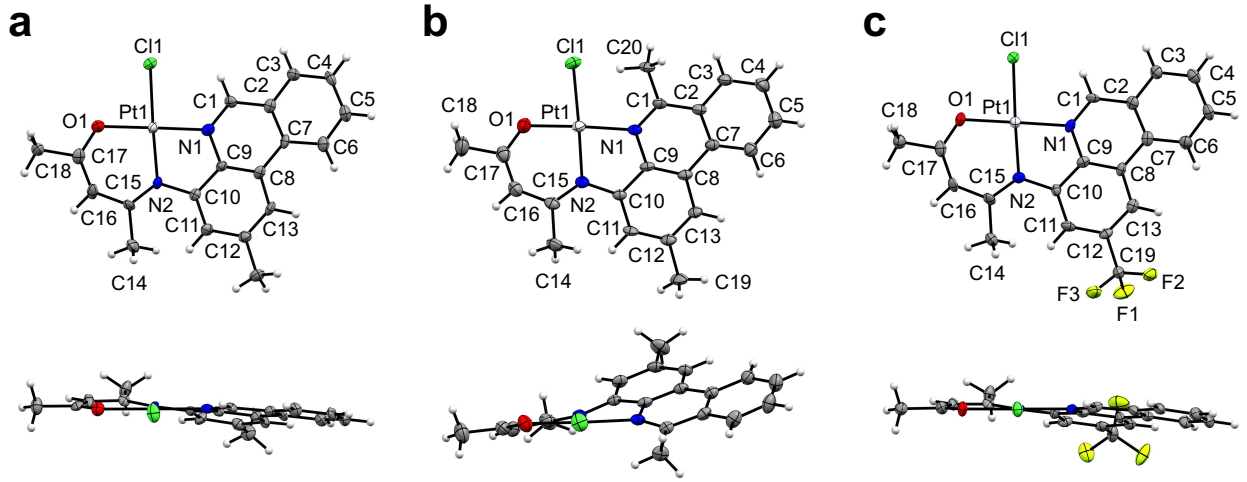

Figure 1. Solid-state structures of (a) **1**, (b) **2** and (c) **4**. Thermal ellipsoids are shown at 50% probability levels. Co-crystallized solvent molecules, when present, and a second molecule of the complex in the asymmetric unit of **2** are omitted for clarity. Selected bond lengths (Å) and bond angles (°): **Complex 1** Pt1–Cl1 2.3166(19); Pt1–O1 1.987(5), Pt1–N1 1.987(6), Pt1–N2

1.997(6), C17-O1 1.288(10); N1−Pt1−Cl1 94.66(18), N1−Pt1−N2 83.1(2), N1−Pt1−O1 179.4(2), N2−Pt1−O1 96.3(2), N2−Pt1−Cl1 177.45(17), O1−Pt1−Cl1 85.91(16). **Complex 2** Pt1–Cl1 2.3341(10), Pt2–Cl2 2.3308(10), Pt1–O1 1.992(3), Pt2–O2 1.986(3), Pt1–N1 2.016(3), Pt2–N3 2.025(3), Pt1–N2 1.987(3), Pt2–N4 1.998(3), C17-O1, 1.297(5), C37-O2 1.283(5); N1−Pt1−Cl1 99.63(9), N3−Pt2−Cl2 100.60(9), N1−Pt1−N2 81.87(13), N3−Pt2−N4 82.26(13), N1−Pt1−O1 174.83(12), N3−Pt2−O2 177.09(13), N2−Pt1−O1 95.47(13), N4−Pt2−O2 95.03(13), N2−Pt1−Cl1 168.24(10), N4−Pt2−Cl2 172.48(9), O1−Pt1−Cl1 83.88(9), O2−Pt2−Cl2 81.97(9). **Complex 4** Pt1–Cl1 2.3305(18); Pt1–O1 1.985(5), Pt1–N1 1.990(6), Pt1–N2 1.995(6), C17-O1 1.278(9); N1−Pt1−Cl1 95.45(18), N1−Pt1−N2 82.6(2), N1−Pt1−O1 179.5(2), N2−Pt1−O1 96.9(2), N2−Pt1−Cl1 177.98(18), O1−Pt1−Cl1 85.07(16).

Electrochemistry

Deprotonation of **L1-L4** and installation on Pt(II) introduces at least partial amido character, which, in the context of pincer-type tridentate ligand scaffolds, should be accessible for electrochemical oxidation.[37] Similarly, low-lying, vacant π* orbitals in the benzannulated ligand framework are anticipated to be accessible for electrochemical reduction.[38] Electrochemical analysis of **L1-L4** (Figure S3) and **1-4** (Figure 2, Figure S4) was therefore undertaken using cyclic voltammetry and differential pulse voltammetry. Largely irreversible anodic and cathodic events are observed, which become more reversible at increased scan rates for **1** and **3**, and to a lesser extent for **2** (Figure S5). Related bis(quiniolinyl)amido, bis(phenanthridinyl)amido and (phenanthridinyl/quinolinyl)amido Pt(II) chloro complexes show closely related redox behavior.[35] Here, however, the oxidation events are shifted to more positive potentials, likely due to the stabilization proffered by the imine/enolato character evident in the solid-state structures.

The cathodic events are similarly accessible at less negative potentials and are much more reversible, with the exception of **2** which presents an electron-donating substituent at the (Me)C=N sub-unit hosting the majority of the orbital density for its LUMO. The results, summarized in Table 1, have been used to estimate experimental HOMO-LUMO gaps (Figure S6).

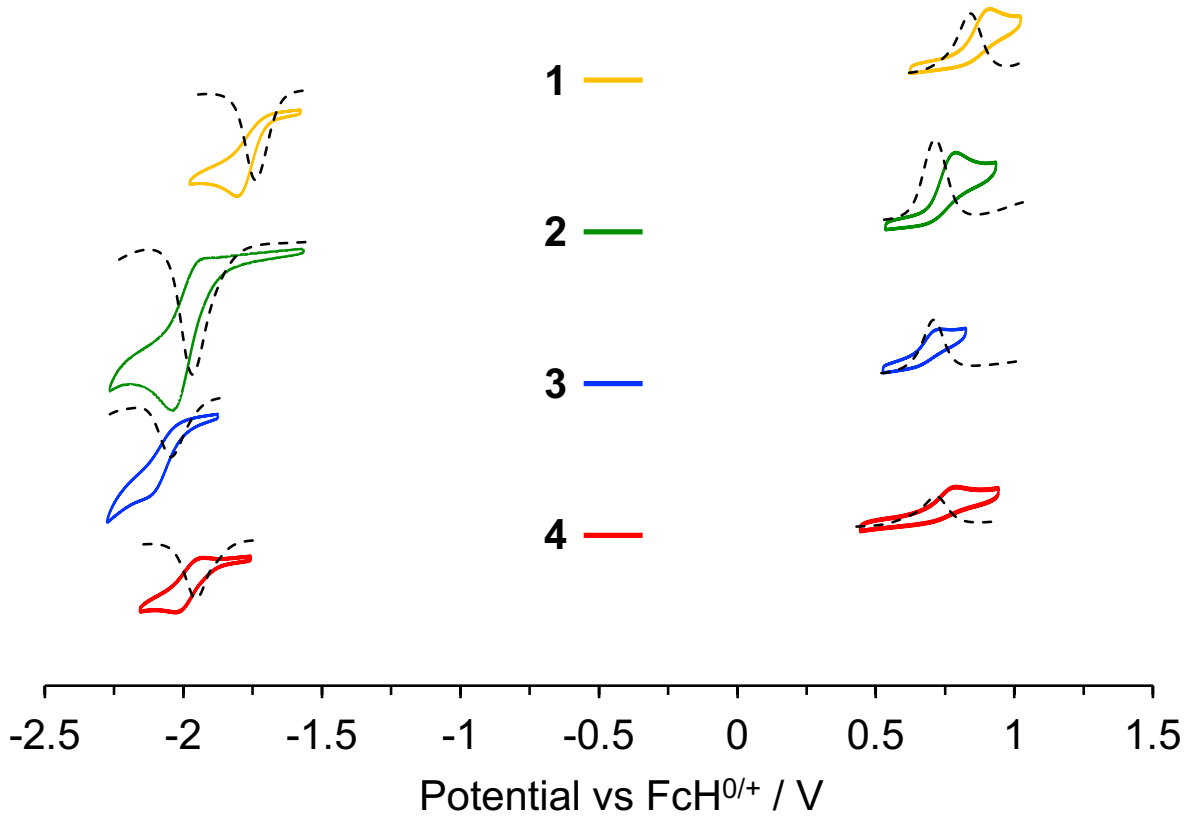

Figure 2. Cyclic voltammograms (solid lines; 100 mV s^{-1}) and differential pulse voltammograms (dashed lines) for **1**-**4** in CH_2Cl_2 containing 0.1 M [nBu$_4$][NPF_6] at 295 K.

Table 1. Electrochemistry data and experimental HOMO/LUMO energies and gaps.

Compound	$E_{1/2}$ / V [a] ($\Delta E_{1/2}$ / V)	$E_{H/L}$ / eV [b]	$\Delta E_{H\text{-}L}$ / eV	E_g [c]
L1	-2.50, 0.64	-5.44/-2.30	3.14	3.22

L2	-2.63, 0.53	-5.33/-2.17	3.16	3.22
L3	-2.53, 0.66	-5.46/-2.27	3.19	3.24
L4	-2.30, 0.82	-5.62/-2.50	3.12	3.20
1	-1.95, 0.72	-5.52/-2.85	2.67	2.68
2	-2.05, 0.71	-5.51/-2.75	2.76	2.74
3	-1.96, 0.71	-5.51/-2.84	2.67	2.70
4	-1.74, 0.85	-5.65/-3.06	2.59	2.61

[a] vs $FcH^{0/+}$ in CH_2Cl_2 at scan rates of 100 mV s^{-1}.

[b] Estimated using equations 1 and 2 (see Supporting Information).

[c] Estimated using equation 3 for **L1-4**, and equation 4 for **1-4** (see Supporting Information).

A general destabilization of the HOMO energies of the ligands is expected in going from electron-withdrawing (CF_3) to electron-releasing (CH_3, *t*Bu) substitution in the 2-position of the phenanthridinyl unit. A further destabilization results from introducing an electron-releasing CH_3 substituent into the 6-position as in **L2** (E_H/eV: **L2** > **L3** ≈ **L1** > **L4**). Consequently, oxidation events occur at lower potentials for **L1**-**L3**, with the most negative oxidation potential for **L2** and most positive oxidation potential observed for **L4**. A similar trend can be discerned in the irreversible cathodic events associated with reduction of the ligands, with **L2** reduced at the most negative potential. This implies that the LUMO energies of the proligands are in the order E_L/eV: **L2** > **L3** ≈ **L1** > **L4**. Overall, however, the HOMO-LUMO gaps estimated from electrochemistry ($\Delta E_{H\text{-}L}$) are quite similar for **L1**-**L4**, indicating that substitution induces similar perturbations to the two frontier molecular orbitals of the ligands. Consistent with this, the UV-Vis spectra of the four proligands are quite similar, except for **2** which presents a broader and slightly blue-shifted λ_{max} (Figure S7).

Upon deprotonation and coordination to the Lewis acidic Pt(II), a shift to more positive potentials is observed for both the oxidation and reduction potentials indicating stabilization of both the HOMO ($\Delta E_{stab.,HOMO}$ / meV: **L1** vs **1**, -180; **L2** vs **2** -190; **L3** vs **3**, -50; **L4** vs **4**, -30) and, even more so, the LUMO $\Delta E_{stab.,LUMO}$ / meV: **L1** vs **1**, -550; **L2** vs **2** -580; **L3** vs **3**, -570; **L4** vs **4**, -560) energies. The experimental HOMO energies of **1-3** are comparable, while in **4**, the HOMO is further stabilized ($\Delta E_{stab.}$ ~ 140 meV vs **1**). In sharp contrast, the LUMO energies mirror the trend observed for the proligands: E_L / eV: **2** < **3** ≈ **1** < **4**, with a larger stabilization energy of 210 meV in **4** relative to **1**. Electronic perturbations by the substituent in the frontier molecular orbital energies are evidently larger for the LUMO than the HOMO in this series.

$d_{Pt}|\pi_L \rightarrow \pi^*_L$

UV-Vis Absorption and Emission Spectroscopy

As noted above, all four complexes are bright orange solids and give rise to similarly colored solutions. UV-Vis absorption spectra (Figure 3a) accordingly exhibit broad and strong bands in the visible region of the electromagnetic spectrum (λ_{max} ~ 460 nm, $\varepsilon > 5\,000$ M^{-1} cm^{-1}) consistent with transitions of charge-transfer character. In addition, two strong transitions are evident in the UV (λ ~ 260 nm, $\varepsilon > 24\,000$ M^{-1} cm^{-1}; λ ~ 350 nm, $\varepsilon >$ 11 000 M^{-1} cm^{-1}), ascribable to ligand-based excitations. Analogous Pt(II) chloride complexes of monoanionic, pincer-type *N*-8-quinolinyl-4-aminophenanthridines[21,22,35] support a mixed [M+L]LCT assignment for the lowest energy manifold. Such N_{amido}-Pt-Cl systems can be compartmentalized in terms of the character of the donor (n_{Cl} + d_{Pt} + n_{Namido}) and acceptor (largely phenanthridine-based π^* orbitals, with significant contribution from the HC=N sub-unit) molecular fragments.

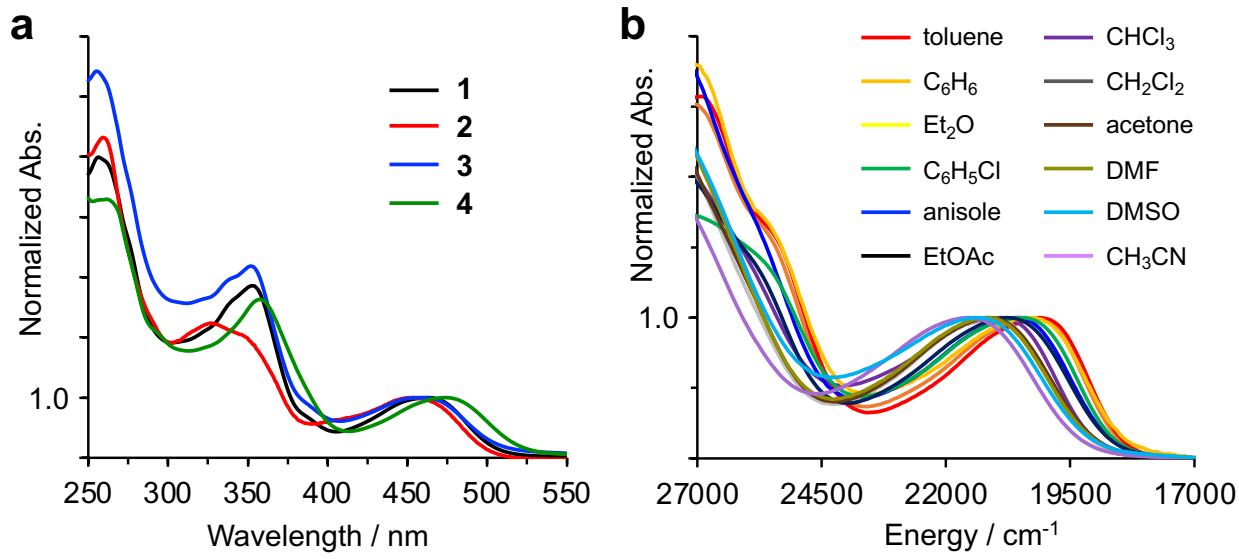

Figure 3. (a) UV-Vis absorption spectra of **1**-**4** in CH_2Cl_2 at 295 K. (b) UV-Vis absorption spectra of **4** in a variety of solvents illustrating the solvatochromism of the lowest energy band.

UV-Vis absorption spectra collected for **4** in a range of solvents support the CT assignment (Figure 3b). The lowest energy absorption exhibits negative solvatochromism, suggesting stabilization of the ground-state relative to the excited state of interest with increasing solvent polarity. Fitting the transition energies to Reichardt's E_N^T function[39] leads to a relatively weak correlation (R^2 = 0.78; Figure S1), which improves when protic and aprotic solvents are treated separately (R^2 = 0.96) suggesting that specific solute-solvent interactions need to be taken into account. Using Catalan's four parameter solvent scale[40] to separate contributions of specific solute-solvent interactions (e.g., solvent acidity/basicity) from non-specific interactions (solvent polarizability/dipolarity) produces a much better correlation between calculated and experimental transition energies (Figure S2). Given solubility constraints on the range of solvents employed, we attribute the hypsochromic shift of λ_{max} in increasingly polar solvents with the most confidence to solvent dipolarity (i.e., solute-solvent dipole interactions) and

solvent acidity (i.e., hydrogen bonding; Table S1-S2). In particular, the large coefficient and positive sign obtained from fitting the solvent dipolarity indicate preferential ground-state stabilization.[39] Increasing solvent dipolarity would be expected to stabilize the larger dipole moment typically associated with an excited state of CT character. However, the [M+L]LCT character of **1**-**4** induces an excited state dipole moment (μ_e) which is not expected to orient in the same direction as the ground state dipole moment (μ_g). The Franck-Condon principle necessitates the solvent to be in a 'frozen' state; that is, the solvent remains in its ground-state equilibrium orientation around the chromophore. This leads to 'orientational strain' on the solvent contributing to the apparent hypsochromic shift in the CT excitation energies with increasing solvent polarity.[41] In contrast, ground state stabilization by solvent acidity is made possible by hydrogen bonding to atom(s) contributing to the HOMO, likely through the chloride. Indeed, incorporation of hydrogen-bonding solvents (e.g., $CHCl_3$) with close contacts to the chloride and oxygen of the ligand is observed in the solid-state structures of **2** (Figure S8).

As with previously reported Pt(II) complexes chelated by monanionic, tridentate *N^N^O* Schiff-base ligands,[28] the novel Pt(II) complexes presented here emit in the orange region of the visible spectrum (λ_{max} ~ 600 nm; Figure 4). Each of complexes **1**, **3** and **4** are brightly emissive, with quantum yields up to 16% in deoxygenated dichloromethane at room temperature (Table 2), superior to those of the archetypal MLCT emitter $[Ru(bpy)_3]^{2+}$ for example,[42] and one to two orders of magnitude larger than those observed for Pt(II) complexes of closely related phenanthridine-based diarylamido ligands.[22] In contrast, the 2,6-dimethyl substituted **2** is only very weakly emissive at room temperature, too weak to record a quantum yield or lifetime reliably. Amongst the other three, complex **4** emits with (marginally) the narrowest band structure (FWHM = 2460 cm^{-1} compared to 2730 cm^{-1} for **3**) and the highest quantum yield. In

comparison, (N^N^O)PtCl complexes based on dipyridylphenolato frameworks were reported to emit at λ_{em} 593-606 nm, with Φ ~1-4 % in the solid-state[27] while those based on Schiff-base ligand frameworks emitted with λ_{em} 686-735 nm (Φ 0.5-4.6 % in fluid solution) for quinoline-based derivatives and λ_{em} 580-636 nm for hydrazone derived analogs (with Φ reaching 0.11 for acetylide derivatives).[28] The luminescence of these three complexes follows mono-exponential decay kinetics, with a lifetime of around 22 μs in each. Values in the microsecond range are typical of phosphorescence from the triplet state in cyclometallated Pt(II) complexes, although most examples tend to be somewhat shorter-lived, typically < 10 μs. Some insight into the longer lifetimes can be gleaned by estimating the radiative k_r and non-radiative Σk_{nr} rate constants from the quantum yields and lifetimes (Table 2). The former are around an order of magnitude lower than found for the brightest Pt(II) emitters (though the brightest tend to be green emitters), but not dissimilar to values for $[Pt(dqpy)Cl]^+$, for example.[REF24] The Σk_{nr} values, meanwhile, are of a magnitude fairly typical for Pt(II) emitters with tridentate ligands.

Given the long lifetimes in fluid solution, it is not surprising to find that the emission is strongly quenched by dissolved molecular oxygen, with bimolecular quenching constants of the order of 10^9 M^{-1} s^{-1} at room temperature. A modest degree of self-quenching is also observed in concentrated solutions, though the self-quenching constants of $1–2 \times 10^8$ M^{-1} s^{-1} are much lower than for systems such as Pt(*N^C^N*-dpyb)Cl and derivatives {dpyb = 1,3-di(2-pyridyl)benzene}.[REF18] Moreover, there is no evidence of excimer emission to lower energy, at elevated concentrations, unlike many of the latter group.

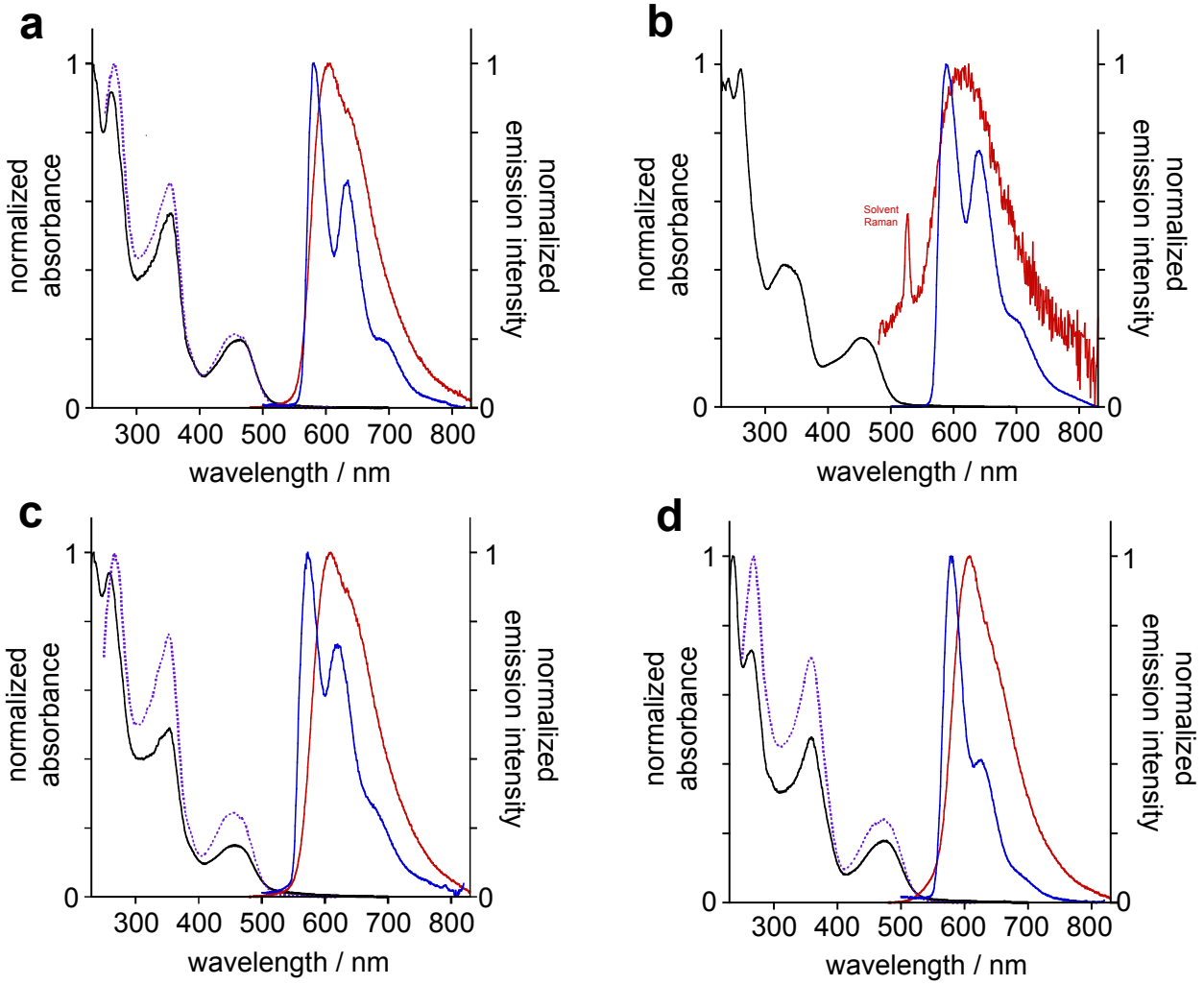

Figure 4. UV-Vis absorption (–), excitation (---) and emission (– at 295 K, – at 77 K) spectra for Pt complexes (a) **1**, (b) **2**, (c) **3** and (d) **4**. (At concentrations suitable for an excitation spectrum, the emission of **2** is too weak to allow one to be recorded).

Table 2. Absorption and emission data of Pt(II) complexes.

	Absorption λ_{max}/nm (ε / M^{-1} cm^{-1})[a]	**Emission** λ_{max}/nm[b]	Φ_{lum} × 10^2 [c]	τ / μs [d]	k_Q^{SQ} / 10^8 M^{-1} s^{-1} [e]	k_Q^{O2} / 10^8 M^{-1} s^{-1}	k_r / 10^3 s^{-1} [f]	Σk_{nr} / 10^3 s^{-1} [f]	**Emission 77 K**[g]	
									λ_{max} / nm	τ / μs
1	261 (27800), 354 (17200), 463 (6030)	604	9.1	23 [0.42]	1.5	11	4.0	40	573, 620, 682sh	64
2	261 (28736),	610	--[h]	--	--	--	--	--	587,	36

	343 (11241), 453 (5424)								640, 700sh	
3	258 (31800), 354 (16500), 459 (5080)	608	6.8	22 [0.41]	2.0	11	3.1	42	573, 620, 682sh	61
4	265 (24600), 360 (16100), 475 (5980)	608	16	24 [0.48]	1.1	9.3	6.7	35	579, 626, 694sh	52

[a] In CH_2Cl_2 at 295 K. (b) In deoxygenated CH_2Cl_2 at 295 K. (c) Measured using $[Ru(bpy)_3]Cl_{2\,(aq)}$ as the standard. (d) Values in parenthesis refer to air-equilibrated solution. (e) Self-quenching rate constant estimated from concentration dependence of lifetime. (f) Radiative k_r and non-radiative Σk_{nr} rate constants calculated assuming that the emitting state is formed with unit efficiency, under which conditions $k_r = \Phi/\tau$ and $\Sigma k_{nr} = (1-\Phi)/\tau$. (g) In diethyl ether / isopentane / ethanol (2:2:1 v/v). (h) The emission intensity of complex **2** is too weak to determine the lifetime or a reliable PLQY.

To better understand the trends in absorption and emission, density functional theory (DFT) modelling of **1**-**4** was performed. Molecular orbital energies from ground-state optimized geometries of **1**-**4** (Figure 5) corroborate the trends in the HOMO-LUMO gap energies gleaned from electrochemistry and electronic absorption spectroscopy. In each case, the HOMO has significant contributions from platinum (~20%), the N^O donor chelate (~45%) and the chloride (~10%), with Pt-N_{amido}/O/Cl π-antibonding character evident in the MO isosurfaces. The LUMO, on the other hand, is largely comprised of the phenanthridinyl π* manifold, with significant contribution from the HC=N fragment (**1** 28, **2** 31, **3** 29, **4** 28%), and additional minor delocalization into the N^O chelate (~15%). The nature of the frontier orbitals is in line with previously studied transition metal complexes supported by ligand frameworks containing phenanthridine with mixed (metal + n_N) HOMO and π_{phen}* LUMO frontier orbitals.[43,44] It is notable that in the HOMOs, there is no orbital density at the 2-position of the phenanthridinyl ring (C_{12}). The weak perturbation in the HOMO energies thus appears to originate from the weak inductive effect of the substituent, through the orbital density at the C_{11} and C_{13} positions. The

CH_3 substituent at the C_1 position did not have any notable effect on the energy of the HOMO of **2** as there is no significant orbital density at C_1 or the adjacent N_2 donor. In comparison, the LUMOs present orbital densities at both C_1 and C_{12} positions; thus, the CF_3 substituent in **4** stabilizes the vacant MO and enhances the electron-accepting character of the LUMO, while the LUMO of **2** is destabilized compared to **1** as a result of hyperconjugation of the CH_3 $\sigma_{C\text{-}H}$ to the phenanthridinyl $\pi^*_{HC=N}$ orbital.

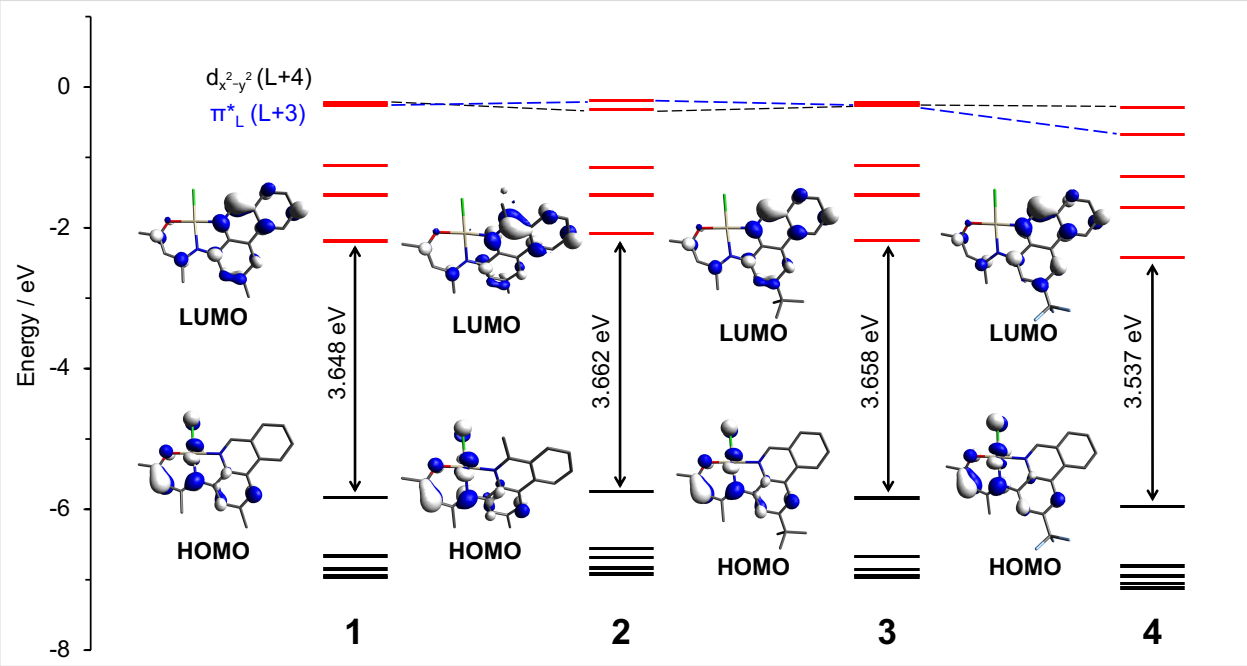

Figure 5. Molecular orbital energy level diagrams, HOMO-LUMO gaps and isosurfaces (isovalue = 0.04) for **1**-**4**.

TDDFT simulations were also carried out. Given the presence of Pt(II), we first investigated the impact of spin-orbit coupling (SOC) on the calculated UV-Vis absorption spectra of a selected complex (**4**). The scalar-only simulated TDDFT spectrum of **4** (Figure S13) suggests only one particle-hole pair involved in the lowest energy manifold of HOMO→LUMO character (97%; Table S12) consistent with a mixed (M+L)LCT assignment. A notable absence

of transitions is observed in the valley region between the lowest energy (~460 nm) and mid-energy (~353 nm) absorption manifolds within the spin-only approximation. Inclusion of SOC (SOC-TDDFT) leads to an increase in the spectral intensity of this region. Previous computational modelling on the UV-Vis absorption spectra of Re(I) carbonyl complexes supported by 8-aminophenanthridines and 4-aminoquinolines indicated that SOC is necessary in accounting for a weak, low-energy transition in the 450-650 nm range of such complexes.[45] In addition, an increasing body of literature supports the necessity of SOC to properly model the absorption spectra of complexes containing heavy elements, providing a mechanism to the direct population of low-lying excited triplet states.[45–48]

SOC-TDDFT simulated spectra for all four complexes calculated using a polarizable continuum of CH_2Cl_2 are in excellent agreement with the experimental UV-Vis absorption spectra (Figures S10-S13, Tables S9-S12). In general, our simulations suggest that two important transitions ($f_{osc} > 0.003$) are responsible for the lowest energy manifold of the experimental UV-Vis spectra. For **1-3**, one weaker, lower-energy (SOC4, $f_{osc} > 0.005$) and a stronger, higher-energy transition (SOC7, $f_{osc} > 0.049$) are prominent, while the weaker SOC4 gains intensity in **4** due to an increased $^1S_1$ contribution (**1-3** < 11%, **4** ~ 40%). Both transitions have largely $^1S_1$ excited singlet-state contributions, while $^3T_2$ states dominates the excited triplet-state. The $^1S_1$ state is largely HOMO→LUMO, that is, (M+L)LCT, in character. The $^3T_2$ excited state, on the other hand, has significant contribution from the HOMO-1→LUMO transitions, which comprises a similar (M+L)LCT character but with increased contribution from Pt (%Pt, HOMO-1: **1** 32, **2** 38, **3** 34, **4** 46) and reduced Cl (%Cl, HOMO-1: **1** 0, **2** 12, **3** 0, **4** 4) contribution. This would suggest that the lowest energy absorption manifold can largely be attributed to HOMO→LUMO transitions, which enables us to estimate the E_g from the λ_{max} of this band. This

explains the excellent agreement between the experimental $\Delta E_{H\text{-}L}$ from electrochemistry and E_g estimated by optical spectroscopy. Thus, the spectral shifts observed between the Pt(II) complexes can be largely attributed to the electronic perturbations identified in the frontier MOs. In either case, relaxation to the lowest-lying triplet state (T_1) is expected prior to radiative decay.

The optimized geometries of the T_1 state, in each case, show a general contraction of the Pt–N_{amido} and Pt–Cl bond distances (Table S4). This is consistent with depopulation of an orbital (HOMO) with Pt-N_{amido}/Pt-Cl antibonding character. The increase in bond order reflects the charge-transfer (CT) character of T_1, as metal-centered states would be expected to result in longer metal-ligand bonds thanks to population of metal-ligand anti-bonding orbitals. Similar π-mixing between ligand π-orbitals and metal *d*-orbitals of appropriate symmetry has been observed in Fe(II) complexes of diarylamido ligands, but not for other metals.[49] In the former, depopulation of a hybrid and highly covalent HOMO with metal-N_{amido} anti-bonding character is similarly thought to result in metal-ligand bond contraction in the CT state, with consequences for CT/MC excited state ordering. In comparison, square planar Pt complexes of dithiolene ligands bearing protonated pyrazine units show diminished dπ-pπ hybridization compared to complexes of lighter elements such as Ni.[50]

Of the four complexes, **2** exhibits the most distortion both experimentally in its solid-state structure, and theoretically in its optimized ground-state and lowest-lying excited triplet state geometry. This is clear from the calculated $\tau_4{}^{\delta}$ parameter (0.16) which indicates a distorted square planar geometry (Figure 6). The anomalously weak emission from **2** can thus be attributed to competitive non-radiative decay pathways made possible by excited state distortions.[19]

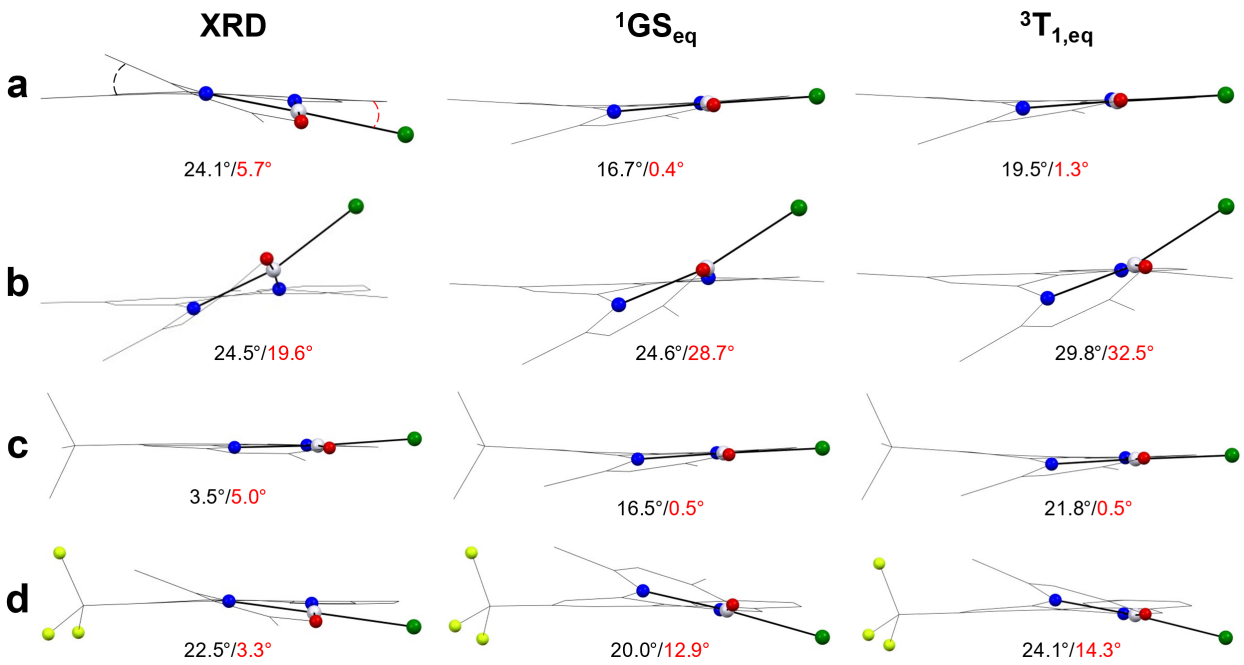

Figure 6. Torsional parameters ($\theta^{\text{phen-}N\text{Acac}}$ and $\theta^{\text{phen-Pt}NN\text{OCl}}$) of the solid-state, optimized ^{1}GS, and $^3T_1$ structures of (a) **1**, (b) **2**, (c) **3** and (d) **4**.

Finally, for the brightest emitter (**4**), we probed the excited state dynamics (ESD) using the ESD module implemented in the ORCA software suite,[51,52] using the optimized geometries of the ground-state (GS, S_0) and lowest-lying triplet excited state (T_1). We first estimated the rate of intersystem crossing (k_{ISC}) of the scalar-only $^1S_1$ (the dominant transition in the visible region) and $^1S_7$ (the dominant transition contributing to the band at 360 nm) states at the ^{1}GS geometry to the lowest-lying excited triplet state at its equilibrium geometry (Table S13). Rapid and efficient population of the triplet state is calculated with average k_{ISC} of 8.870×10^{12} s^{-1} ($^1S_1\rightarrow{}^3T_1$) and 1.020×10^{13} s^{-1} ($^7S_1\rightarrow{}^3T_1$). This suggests a strong coupling between these states and the presumably emissive $^3T_1$ state, consistent with the strong mixing between the singlet and triplet states through the influence of SOC, evident in the UV-Vis absorption spectra as discussed above. SOC-TDDFT simulations also predict strong mixing between $^1S_1$ and $^3T_2$, both of which contribute significantly to the predicted strong, low-energy absorptions in the calculated SOC-

TDDFT spectrum (Figure S13, Table S12), and which both exhibit (M+L)LCT character. This suggests that $^3T_2$ is also populated, which likely undergoes rapid internal conversion to $^3T_1$ (Figure S14).

We also simulated the phosphorescence spectra and decay parameters for **4**. In general, the spectra of **4** at 295 K (Figure S15) and 77 K (Figure S16) were faithfully reproduced with errors of < 0.2 eV. The vibrational progression observed at 77 K that appears as a low-energy shoulder at 295 K is reproduced in both calculated spectra, indicating the molecule retains rigidity in solution at 295 K with only minimal distortion as shown by similar values for τ_4^{δ} for both ^{1}GS and $^3T_{1,eq}$. In contrast, the emission spectrum of **2** is broad and weak at 295 K, but resembles those of **1**, **3** and **4** at 77 K (Figure S17). This implies that significant distortions occur at higher temperature, in line with the weakness of the emission. Spin density maps reveal a similar (M+L)LCT character of the emissive triplet state (Figure S18).

Conclusions

In summary, multidentate N^N^O β-enaminoketonato ligands bearing benzannulated *N*-heterocyclic phenanthridinyl donor arms can be used to prepare new luminescent Pt(II) complexes under mild conditions. The substitution pattern on the phenanthridinyl ligand lends control over emissive properties by impacting molecular rigidity rather than ligand electronics, and bright orange emission is observed from three of the four complexes at room temperature, with quantum yields up to 16% for the CF_3-substituted congener **4**. In contrast, methyl substitution at the 6-position of the phenanthridinyl system promotes competitive non-radiative decay, which was traced back to enhanced distortions in both the ground-state and excited state. Compared with closely related quinoline-containing phenolate N^N^O Pt(II) complexes,[28] the

higher quantum yields suggests that nac-ac ligand scaffolds and benzannulated acceptor arms can be combined to access improved photophysical properties under comparably simple synthetic conditions.

Experimental Section

Air-sensitive manipulations were carried out in a N_2-filled glove box or using standard Schlenk techniques under Ar. Platinum dichloride (Millipore Sigma) and other common reagents were purchased from commercial suppliers and used without further purification. **L1**-**L4**, **3** and **4** were prepared according to literature procedures.[33,34] Organic solvents were dried and distilled using appropriate drying agents. 1- and 2D NMR spectra were recorded on a Bruker Avance 300 MHz spectrometer or a Bruker Avance 500 MHz spectrometer. ^{1}H and ^{13}C{^{1}H} NMR spectra were referenced to residual solvent peaks. High resolution mass spectra were recorded using a Bruker microOTOF-QIII. Attenuated total reflectance infrared spectroscopy (ATR-IR) was collected using a Bruker Invenio R FTIR or a Perkin Elmer Spectrum Two FTIR spectrometer.

Synthesis of [Pt(L1)Cl], 1: A solution of **L1** (58.7 mg, 0.113 mmol) in THF (3.5 mL) was added to a suspension of $PtCl_2$ (61.8 mg, 0.232 mmol), Ag_2O (29.3 mg, 0.126 mmol) and 4 Å molecular sieves (180 mg) in THF (3.5 mL). The mixture was protected from light and heated in an oil bath set to 60 °C for 16 h. The mixture was then filtered over Celite then the solvent was evaporated to isolate an orange solid compound. The product was purified by precipitation from a $CHCl_3$ solution using petroleum ether. Isolated yield = 36.2 g (34%). ^{1}H NMR ($CDCl_3$, 500 MHz, 22 °C): δ 9.97 (s, 1H, $^{3}J_{PtH}$ = 40 Hz; C_1H), 8.46 (d, $^{3}J_{HH}$ = 8.3 Hz, 1H; C_6H), 8.03 (d, $^{3}J_{HH}$ = 8.0 Hz, 1H; C_3H), 7.95

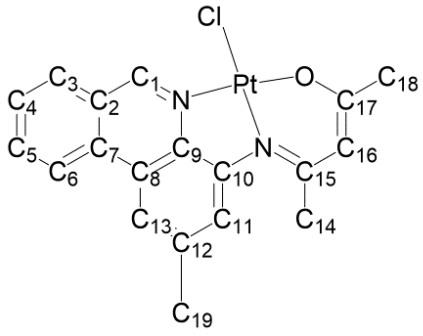

(m, 1H; C_5H), 7.81 (s, 1H; $C_{13}H$), 7.72 (m, 1H; C_4H), 7.53 (s, 1H; $C_{11}H$), 5.28 (s, 1H; $C_{16}H$), 2.62 (s, 3H; $C_{19}H$), 2.42 (s, 3H; $C_{20}H$), 2.07 ppm (s, 3H; $C_{14}H$). $^{13}C\{^1H\}$ NMR ($CDCl_3$, 125 MHz, 22 °C): δ 179.8 (C_{16}), 158.1 (C_{18}), 154.7 (C_1), 148.8 (C_{10}), 139.1 (C_{12}), 138.9 (C_9), 133.5 (C_5), 131.9 (C_2), 130.0 (C_3), 128.9 (C_4), 126.3 (C_8), 125.5 (C_7), 122.6 (C_6), 122.6 (C_{11}), 117.9 (C_{13}), 106.7 (C_{16}), 26.2 (C_{14}), 25.7 (C_{18}), 22.6 ppm (C_{19}). HRMS (ESI-TOF) m/z: $[M + Na]^+$ Calcd for $[C_{19}H_{17}ClN_2OPt+Na]^+$ 542.0571; Found 542.0532.

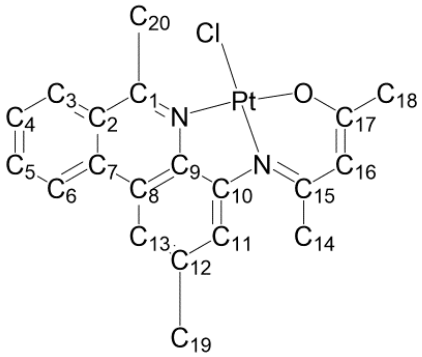

Synthesis of [Pt(L2)Cl], 2: An identical procedure to the preparation of **1** was followed using a solution of **L2** (61.2 mg, 0.115 mmol) in THF (3.5 mL), and a suspension of $PtCl_2$ (0.0590 g, 0.222 mmol), Ag_2O (0.0313 g, 0.135 mmol) and 4 Å molecular sieves (0.122 g) in THF (3.5 mL). After precipitation from $CHCl_3$, the supernatant was further concentrated, and more product was following diffusion of diethylether vapors into the solution. Isolated yield = 0.0519 g (49%). ^1H NMR ($CDCl_3$, 500 MHz, 22 °C): δ 8.51 (d, $^3J_{HH}$ = 8.4 Hz, 1H; C_6H), 8.21 (d, $^3J_{HH}$ = 8.4 Hz, 1H; C_3H), 7.92 (ddd, $^3J_{HH}$ = 8.4, 7.6 Hz, $^4J_{HH}$ = 1.0 Hz, 1H; C_5H), 7.78 (s; 1H; $C_{13}H$), 7.69 (ddd; $^3J_{HH}$ = 8.7, 7.7 Hz; $^4J_{HH}$ = 0.9 Hz; 1H; C_4H), 7.19 (s; 1H; $C_{11}H$), 5.27 (s; 1H; $C_{16}H$), 3.53 (s; 1H; $C_{19}H$), 2.56 (s; 1H; $C_{20}H$), 2.28 (s; 1H; $C_{14}H$), 2.06 (s; 1H; $C_{18}H$). 13C{1H} NMR (CDCl3, 125 MHz, 22 °C): δ 179.9 (C_{19}), 167.8 (C_1), 158.3 (C_{17}), 148.8 (C_{10}), 140.1 (C_9), 137.7 (C_{12}), 133.0 (C_5), 131.4 (C_7), 128.8 (C_4), 127.9 (C_3), 127.1 (C_2), 124.6 (C_8), 122.7 (C_6), 121.0 (C_{11}), 117.4 (C_{13}), 106.5 (C_{16}), 26.8 (C_{19}), 25.3 (C_{18}), 23.7 (C_{14}), 22.2 ppm (C_{20}). HRMS (ESI-TOF) m/z: $[M]^+$ Calcd for $[C_{20}H_{19}N_2OPt]^+$ 498.1142; Found 498.1130.

X-Ray Crystallography Experimental Details

X-ray crystal structure data was collected from multi-faceted crystals of suitable size and quality selected from a representative sample of crystals of the same habit using an optical microscope. Crystals were mounted on MiTiGen loops and data collection carried out in a cold stream of nitrogen (150 K; Bruker D8 QUEST ECO). Diffractometer manipulations were carried out using Bruker APEX3 software.[53] Structure solution and refinement was performed using XS, XT and XL software, embedded within the OLEX2.[54] For each structure, the absence of additional symmetry was confirmed using ADDSYM incorporated in the PLATON program.[55]

Crystal structure data for 1 (CCDC 2100576): X-ray quality crystals were grown following diffusion of diethyl ether vapor into $CHCl_3$ at room temperature. Crystal structure parameters: $C_{19}H_{17}ClN_2OPt$ 519.89 g/mol, monoclinic, space group $P2_1/n$; a = 9.2499(5) Å, b = 11.5853(6) Å, c = 15.3470(8) Å, $\alpha = \gamma = 90°$, β = 103.623(2)°, V = 1598.36(15) Å^3; Z = 4, ρ_{calcd} = 2.160 g cm^{-3}; crystal dimensions 0.16 x 0.14 x 0.02 mm; diffractometer Bruker D8 QUEST ECO CMOS; Mo K_α radiation, 150(2) K, $2\theta_{max}$ = 2.731 to 24.790°; 23441 reflections, 2739 independent (R_{int} = 0.0642), direct methods; absorption coeff (μ = 8.954 mm^{-1}), absorption correction semi-empirical from equivalents (SADABS); refinement (against F_o^2) with SHELXTL V6.1, 220 parameters, 0 restraints, R_1 = 0.0351 ($I > 2\sigma$) and wR_2 = 0.0754 (all data), Goof = 1.121, residual electron density 1.745/−1.521 e Å^{-3}.

Crystal structure data for 2 (CCDC 2100577): X-ray quality crystals were grown following diffusion of diethyl ether vapor into $CHCl_3$ at room temperature. Crystal structure parameters: $C_{21}H_{20}Cl_4N_2OPt$ 653.28 g/mol, triclinic, space group $P\bar{1}$; a = 11.0564(7) Å, b = 14.0350(9) Å, c = 16.4321(10) Å, α = 113.018(2)°, β = 99.705(2)°, γ = 100.551(2)°, V = 2224.4(2) Å^3; Z = 4, ρ_{calcd} = 1.951 g cm^{-3}; crystal dimensions 0.35 x 0.14 x 0.06 mm; diffractometer Bruker D8 QUEST ECO CMOS; Mo K_α radiation, 150(2) K, $2\theta_{max}$ = 2.550 to 30.591°; 61734 reflections,

13610 independent (R_{int} = 0.0468), direct methods; absorption coeff (μ = 6.804 mm^{-1}), absorption correction semi-empirical from equivalents (SADABS); refinement (against F_o^2) with SHELXTL V6.1, 531 parameters, 0 restraints, R_1 = 0.0335 ($I > 2\sigma$) and wR_2 = 0.652 (all data), Goof = 1.044, residual electron density 1.784/-1.569 e $Å^{-3}$.

Crystal structure data for 4 (CCDC 2100578): X-ray quality crystals were grown following diffusion of diethyl ether vapor into $CHCl_3$ at room temperature. Crystal structure parameters: $C_{19}H_{14}ClF_3N_2OPt$ 573.86 g/mol, monoclinic, space group $P2_1/n$; a = 9.5576(6) Å, b = 11.5940(7) Å, c = 15.7469(10) Å, $\alpha = \gamma = 90°$, β = 105.381(2)°, V = 1682.43(18) $Å^3$; Z = 4, ρ_{calcd} = 2.266 g cm^{-3}; crystal dimensions 0.1 x 0.08 x 0.05 mm; diffractometer Bruker D8 QUEST ECO CMOS; Mo K_α radiation, 150(2) K, $2\theta_{max}$ = 2.683 to 27.553°; 40565 reflections, 3880 independent (R_{int} = 0.0828), direct methods; absorption coeff (μ = 8.543 mm^{-1}), absorption correction semi-empirical from equivalents (SADABS); refinement (against F_o^2) with SHELXTL V6.1, 231 parameters, 0 restraints, R_1 = 0.0436 ($I > 2\sigma$) and wR_2 = 0.0844 (all data), Goof = 1.115, residual electron density 2.469/-2.433 e $Å^{-3}$.

UV-Visible absorption and luminescence measurements

Absorption spectra were measured on a Biotek Instruments XS spectrometer, using quartz cuvettes of 1 cm pathlength. Steady-state luminescence spectra were measured using a Jobin Yvon FluoroMax-2 spectrofluorimeter, fitted with a red-sensitive Hamamatsu R928 photomultiplier tube; the spectra shown are corrected for the wavelength dependence of the detector, and the quoted emission maxima refer to the values after correction. Samples for emission measurements were contained within quartz cuvettes of 1 cm pathlength modified with appropriate glassware to allow connection to a high-vacuum line. Degassing was achieved via a minimum of three freeze-pump-thaw cycles whilst connected to the vacuum manifold; final

vapor pressure at 77 K was < 5×10^{-2} mbar, as monitored using a Pirani gauge. Luminescence quantum yields were determined using $[Ru(bpy)_3]Cl_2$ in aqueous solution as the standard (Φ = 0.04±0.002. The estimated uncertainty on the quantum yields obtained in this way on the instrumentation employed is up to ±20%.

Luminescence lifetimes of the complexes in air-equilibrated solutions were measured by time-correlated single-photon counting, following excitation at 405 nm with a pulsed-diode laser. The emitted light was detected at 90° using a Peltier-cooled R928 PMT after passage through a monochromator. The estimated uncertainty in the quoted lifetimes is ± 10% or better. Lifetimes in deoxygenated solution and at 77 K were measured following excitation with a microsecond-pulsed xenon lamp and detection using the same PMT operating in multichannel scaling mode. For all measurements, the decays were much longer than the instrument response, and data were analysed by tail fitting to the following equation (rather than by deconvolution of the response function):

$$I(t) = I(0) \exp(-kt) + c$$

where $I(t)$ is the intensity of light detected at time t, k is the first-order rate constant for decay (k = 1/t), and c is a constant reflecting the intrinsic "dark count" during the measurement. The estimated uncertainty in the quoted lifetimes is ±10%. Bimolecular rate constants for quenching by molecular oxygen, k_Q, were determined from the lifetimes in degassed and air-equilibrated solution, taking the concentration of oxygen in CH_2Cl_2 at 0.21 atm O_2 to be 2.2 mmol dm^{-3}.

Computational Modeling. Modeling of all complexes were carried out using Orca version 4.2.1.[51,52] The resolution-of-identity with chain-of-spheres approximation (RIJCOSX[56]) as

implemented in Orca was used to speed up all calculations. Geometry optimizations were performed in the gas phase with the dispersion corrected (D3BJ[57,58]) PBE0[59–61] functional and the def2-TZVP(-f)[62,63] on all atoms and the corresponding ECP basis set on Pt. The def2/J auxiliary basis sets on all atoms were used in the density fitting. The $^1S_{0,eq}$, $^1S_{1,eq}$, and $^3T_{1,eq}$ geometries were optimized for **4** to understand the deactivation mechanisms in the Pt(II) complexes, as the CF_3-substituted complex had the highest quantum yield. Only $^1S_{0,eq}$ and $^3T_{1,eq}$ geometries were optimized for **1**, **2** and **3**. The starting input for ground state ($^1S_{0,eq}$) geometries were obtained from the solid-state structure coordinates. The $^1S_{1,eq}$ geometry was optimized with either full time-dependent DFT (TDDFT) or Tamm-Dancoff/TDDFT[64] approaches. The following SCF and geometry convergence criteria, DFT grids, COSX grids were used for the optimizations: tightscf, tightopt, grid5, finalgrid6, intaccx (4.34,4.34,4.67), and gridx (2,2,2). Frequency calculations were carried to confirm that all geometries are at a minimum.

Single point calculations were carried using the same dispersion corrected PBE0 functional and inclusion of implicit solvation using the solvation model based on density (SMD[65], solvent = CH_2Cl_2) on gas-phase optimized geometries. However, to best account for scalar relativistic effects, we employed the zeroth order approximation (ZORA[66]), ZORA-optimized all-electron relativistic (ZORA-def2-TZVP[63] on H, C, N, O, F, and Cl; SARC-ZORA-TZVP on Pt) and auxiliary basis sets (SARC/J[67,68]). We used the same SCF convergence criteria and COS-X grid for all single points (tightscf; intaccx 4.34, 4.34, 4.67; gridx 2,2,2), while the DFT integration grids were increased to grid6 and finalgrid7. We also increased the grid around Pt (specialgridintacc 9). Time-dependent DFT (TDDFT) was used to predict the first 50 $^1S_{n,FC}\leftarrow{}^1S_{0,eq}$ and $^3T_{n,FC}\leftarrow{}^1S_{0,eq}$ excitations to simulate the UV-Vis spectra of the complexes

without spin-orbit correction. In addition, we also predicted the extent of SOC effects by allowing mixing of ^1S_n and ^3T_n states as implemented in Orca.

Improving a previously published[29] protocol using the ESD module implemented on Orca version 4.2.1, the following photophysical parameters: (1) $E^{vert,adb}$, (2) $E^{vert,abs}$, (3) $E^{vert,phos}$, and (4) λ_T were calculated at the same level of theories described above. Additional photophysical parameters such as the 5) phosphorescence rate constants (k^{Phos}), 6) intersystem crossing rate (k^{ISC}) were calculated. The three substates (M_S = -1, 0, +1) of the lowest excited triplet state were considered in estimating k^{Phos} and k^{ISC} at the default temperature, 298 K, and 77 K. For k^{ISC}, we consider the ground state optimized geometry as the geometry of the populated excited singlet states initially populated upon light excitation. This is performed for both $^1S_1(^1GS)$ and $^1S_7(^1GS)$, as these have the strongest oscillator strengths in the absorbance bands at 475 and 360 nm, respectively. The final geometry is of the lowest-lying excited triplet state. For the k^{Phos}, initial and final geometries are of the lowest-lying excited triplet state and ground state, respectively.

ASSOCIATED CONTENT

Supporting Information. Additional UV-Vis absorption and emission spectra; computational data tables; multi-nuclear NMR spectra of all new compounds; crystallographic information files containing all X-ray data. CCDC 2100576-2100578 contain the supplementary crystallographic data for this paper. The data can be obtained free of charge from The Cambridge Crystallographic Data Center via www.ccdc.cam.ac.uk/structures.

The following files are available free of charge:

Supporting Information File (PDF)

Combined Crystallographic Information File (CIF)

AUTHOR INFORMATION

Corresponding Authors

David E. Herbert (david.herbert@umanitoba.ca)

J. A. Gareth Williams (j.a.g.williams@durham.ac.uk)

ORCIDs

Issiah B. Lozada: 0000-0002-1689-2918

J. A. Gareth Williams: 0000-0002-4688-3000

David E. Herbert: 0000-0001-8190-2468

Author Contributions

The manuscript was written through contributions of all authors. All authors have given approval to the final version of the manuscript.

Conflicts of Interest

There are no conflicts of interest to declare.

ACKNOWLEDGMENTS

The following sources of funding are gratefully acknowledged: the Natural Sciences Engineering Research Council of Canada for a Discovery Grant to DEH (RGPIN-2014-03733); the Canadian Foundation for Innovation and Research Manitoba for an award in support of an X-ray diffractometer (CFI #32146); the University of Manitoba for the Bert & Lee Friesen Graduate Scholarship (IBL) and GETS support.

REFERENCES

1 W.-Y. Wong and C.-L. Ho, *Coord Chem Rev*, 2009, **253**, 1709–1758.
2 H. Yersin, A. F. Rausch, R. Czerwieniec, T. Hofbeck and T. Fischer, *Coord. Chem. Rev.*, 2011, **255**, 2622–2652.
3 J. Kalinowski, V. Fattori, M. Cocchi and J. A. G. Williams, *Coord. Chem. Rev.*, 2011, **255**, 2401–2425.
4 C. Cebrian and M. Mauro, *Beilstein J Org Chem*, 2018, **14**, 1459–1481.
5 E. Baggaley, J. A. Weinstein and J. A. G. Williams, *Coord Chem Rev*, 2012, **256**, 1762–1785.
6 M. Mauro, A. Aliprandi, D. Septiadi, N. S. Kehr and L. De Cola, *Chem. Soc. Rev.*, 2014, **43**, 4144–4166.
7 Y. Chen, R. Guan, C. Zhang, J. Huang, L. Ji and H. Chao, *Coord Chem Rev*, 2016, **310**, 16–40.
8 Q. Zhao, F. Li and C. Huang, *Chem. Soc. Rev.*, 2010, **39**, 3007–3030.
9 V. W.-W. Yam and A. S.-Y. Law, *Coord Chem Rev*, 2020, **414**, 213298.
10 P.-T. Chou, Y. Chi, M.-W. Chung and C.-C. Lin, *Coord Chem Rev*, 2011, **255**, 2653–2665.
11 K. Li, G. S. Ming Tong, Q. Wan, G. Cheng, W.-Y. Tong, W.-H. Ang, W.-L. Kwong and C.-M. Che, *Chem. Sci.*, 2016, **7**, 1653–1673.
12 A. Haque, L. Xu, R. A. Al-Balushi, M. K. Al-Suti, R. Ilmi, Z. Guo, M. S. Khan, W.-Y. Wong and P. R. Raithby, *Chem. Soc. Rev.*, 2019, **48**, 5547–5563.
13 E. C. Constable, R. P. G. Henney, T. A. Leese and D. A. Tocher, *J. Chem. Soc. Dalton Trans. Inorg. Chem. 1972-1999*, 1990, 443–9.
14 S.-W. Lai, M. C.-W. Chan, T.-C. Cheung, S.-M. Peng and C.-M. Che, *Inorg. Chem.*, 1999, **38**, 4046–4055.
15 C. F. Harris, D. A. K. Vezzu, L. Bartolotti, P. D. Boyle and S. Huo, *Inorg. Chem.*, 2013, **52**, 11711–11722.
16 Z. Wang, E. Turner, V. Mahoney, S. Madakuni, T. Groy and J. Li, *Inorg. Chem.*, 2010, **49**, 11276–11286.
17 D. A. K. Vezzu, D. Ravindranathan, A. W. Garner, L. Bartolotti, M. E. Smith, P. D. Boyle and S. Huo, *Inorg. Chem.*, 2011, **50**, 8261–8273.
18 J. A. G. Williams, *Chem. Soc. Rev.*, 2009, **38**, 1783–1801.
19 A. F. Rausch, L. Murphy, J. A. G. Williams and H. Yersin, *Inorg. Chem.*, 2012, **51**, 312–319.
20 K. Hanson, L. Roskop, P. I. Djurovich, F. Zahariev, M. S. Gordon and M. E. Thompson, *J. Am. Chem. Soc.*, 2010, **132**, 16247–16255.
21 P. Mandapati, J. D. Braun, C. Killeen, R. L. Davis, J. A. G. Williams and D. E. Herbert, *Inorg Chem*, 2019, **58**, 14808–14817.
22 P. Mandapati, J. D. Braun, I. B. Lozada, J. A. G. Williams and D. E. Herbert, *Inorg. Chem.*, 2020, **59**, 12504–12517.
23 G. T. Morgan and F. H. Burstall, *J. Chem. Soc.*, 1934, 1498–500.
24 K. L. Garner, L. F. Parkes, J. D. Piper and J. A. G. Williams, *Inorg. Chem.*, 2010, **49**, 476–487.
25 J. A. Bailey, M. G. Hill, R. E. Marsh, V. M. Miskowski, W. P. Schaefer and H. B. Gray, *Inorg. Chem.*, 1995, **34**, 4591–4599.
26 D. A. Bardwell, J. G. Crossley, J. C. Jeffery, A. G. Orpen, E. Psillakis, E. E. M. Tilley and M. D. Ward, *Polyhedron*, 1994, **13**, 2291–300.

27 C.-C. Kwok, H. M. Y. Ngai, S.-C. Chan, I. H. T. Sham, C.-M. Che and N. Zhu, *Inorg. Chem.*, 2005, **44**, 4442–4444.
28 E. V. Puttock, J. D. Fradgley, D. S. Yufit and J. A. G. Williams, *Dalton Trans.*, 2019, **48**, 15012–15028.
29 R. Mondal, I. B. Lozada, R. L. Davis, J. A. G. Williams and D. E. Herbert, *Inorg Chem*, 2018, **57**, 4966–4978.
30 R. Mondal, I. B. Lozada, R. L. Davis, J. A. G. Williams and D. E. Herbert, *J. Mater. Chem. C*, 2019, **7**, 3772–3778.
31 R. Mondal, P. K. Giesbrecht and D. E. Herbert, *Polyhedron*, 2016, **108**, 156–162.
32 R. H. Holm, G. W. Everett Jr. and Animesh. Chakravorty, *Prog. Inorg. Chem.*, 1966, **7**, 83–214.
33 I. B. Lozada, B. Huang, M. Stilgenbauer, T. Beach, Z. Qiu, Y. Zheng and D. E. Herbert, *Dalton Trans.*, 2020, **49**, 6557–6560.
34 I. B. Lozada, R. J. Ortiz, J. D. Braun, J. A. G. Williams and D. E. Herbert, *in preparation*.
35 P. Mandapati, P. K. Giesbrecht, R. L. Davis and D. E. Herbert, *Inorg Chem*, 2017, **56**, 3674–3685.
36 M. H. Reineke, M. D. Sampson, A. L. Rheingold and C. P. Kubiak, *Inorg. Chem.*, 2015, **54**, 3211–3217.
37 J. J. Davidson, J. C. DeMott, C. Douvris, C. M. Fafard, N. Bhuvanesh, C.-H. Chen, D. E. Herbert, C.-I. Lee, B. J. McCulloch, B. M. Foxman and O. V. Ozerov, *Inorg. Chem.*, 2015, **54**, 2916–2935.
38 P. K. Giesbrecht, D. B. Nemez and D. E. Herbert, *Chem Commun*, 2018, **54**, 338–341.
39 C. Reichardt, *Chem. Rev.*, 1994, **94**, 2319–2358.
40 J. Catalán, *J. Phys. Chem. B*, 2009, **113**, 5951–5960.
41 G. Van der Zwan and J. T. Hynes, *J. Phys. Chem.*, 1985, **89**, 4181–4188.
42 J. V. Caspar and T. J. Meyer, *J. Am. Chem. Soc.*, 1983, **105**, 5583–5590.
43 I. B. Lozada, T. Murray and D. E. Herbert, *Polyhedron*, 2019, **161**, 261–267.
44 J. D. Braun, I. B. Lozada, C. Kolodziej, C. Burda, K. M. E. Newman, J. van Lierop, R. L. Davis and D. E. Herbert, *Nat. Chem.*, 2019, **11**, 1144–1150.
45 S. Gaire, R. J. Ortiz, B. R. Schrage, I. B. Lozada, P. Mandapati, A. J. Osinski, D. E. Herbert and C. J. Ziegler, *J. Organomet. Chem.*, 2020, **921**, 121338.
46 A. R. G. Smith, P. L. Burn and B. J. Powell, *ChemPhysChem*, 2011, **12**, 2429–2438.
47 E. Ronca, F. De Angelis and S. Fantacci, *J. Phys. Chem. C*, 2014, **118**, 17067–17078.
48 C. Gourlaouen and C. Daniel, *Dalton Trans*, 2014, **43**, 17806–17819.
49 J. D. Braun, I. B. Lozada and D. E. Herbert, *Inorg. Chem.*, 2020, **59**, 17746–17757.
50 M. Hayashi, Y. Takahashi, Y. Yoshida, K. Sugimoto and H. Kitagawa, *J. Am. Chem. Soc.*, 2019, **141**, 11686–11693.
51 F. Neese, *WIREs Comput. Mol. Sci.*, 2012, **2**, 73–78.
52 F. Neese, *WIREs Comput. Mol. Sci.*, 2018, **8**, e1327.
53 Bruker-AXS, *APEX3 v2016.1-0*, Madison, Wisconsin, USA, 2016.
54 O. V. Dolomanov, L. J. Bourhis, R. J. Gildea, J. A. K. Howard and H. Puschmann, *J. Appl. Crystallogr.*, 2009, **42**, 339–341.
55 A. L. Spek, *Acta Cryst*, 2009, **D65**, 148–155.
56 F. Neese, F. Wennmohs, A. Hansen and U. Becker, *Chem. Phys.*, 2009, **356**, 98–109.
57 S. Grimme, S. Ehrlich and L. Goerigk, *J. Comput. Chem.*, 2011, **32**, 1456–1465.
58 S. Grimme, J. Antony, S. Ehrlich and H. Krieg, *J. Chem. Phys.*, 2010, **132**, 154104.

59 M. Ernzerhof and G. E. Scuseria, *J. Chem. Phys.*, 1999, **110**, 5029–5036.
60 J. P. Perdew, K. Burke and M. Ernzerhof, *Phys. Rev. Lett.*, 1996, **77**, 3865–3868.
61 C. Adamo and V. Barone, *J. Chem. Phys.*, 1999, **110**, 6158–6170.
62 D. Andrae, U. Huermann, M. Dolg, H. Stoll and H. Preu, *Theor. Chim. Acta*, 1990, **77**, 123–141.
63 F. Weigend and R. Ahlrichs, *Phys. Chem. Chem. Phys.*, 2005, **7**, 3297.
64 S. Hirata and M. Head-Gordon, *Chem. Phys. Lett.*, 1999, **314**, 291–299.
65 A. V. Marenich, C. J. Cramer and D. G. Truhlar, *J Phys Chem B*, 2009, **113**, 6378–6396.
66 C. van Wüllen, *J. Chem. Phys.*, 1998, **109**, 392–399.
67 F. Weigend, *Phys. Chem. Chem. Phys.*, 2006, **8**, 1057.
68 D. A. Pantazis, X.-Y. Chen, C. R. Landis and F. Neese, *J. Chem. Theory Comput.*, 2008, **4**, 908–919.